ACS Sustainable Chemistry & Engineering

Research Article

pubs.acs.org/journal/ascecg

Rapid Synthesis of C-TiO_2: Tuning the Shape from Spherical to Rice Grain Morphology for Visible Light Photocatalytic Application

Balaji Sambandam,[†] Anupama Surenjan,[‡] Ligy Philip,[‡] and Thalappil Pradeep*,[†]

[†]DST Unit of Nanoscience and Thematic Unit of Excellence, Department of Chemistry, Indian Institute of Technology Madras, Chennai 600036, India

[‡]Department of Civil Engineering, Indian Institute of Technology Madras, Chennai 600036, India

Supporting Information

ABSTRACT: Visible light-active carbon-loaded anatase TiO_2 (C-TiO_2) nanocrystals of spherical, distorted spherical, rice grain and hexagonal morphologies, with a particle size range of 50−70 nm, have been synthesized by a rapid microwave-assisted route in the solution state. The morphology of these materials is greatly tuned at low concentrations of the precursors used. The absorption band gaps (E_{gap}) are shifted to the visible region due to C loading, and the distorted spherical C-TiO_2 exhibits a maximum energy shift relative to pure TiO_2. Carbon gets deposited predominantly on the surface as graphitic carbon, in the preparative conditions, as confirmed by X-ray photoelectron, scanning electron microscopy elemental mapping and Raman spectroscopic studies. The rapid degradation of an endocrine disrupting agent and a persistent pollutant in wastewater, carbamazepine, by the rice grain shaped C-TiO_2 is attributed to the large surface area (229 m^2/g) of the particles and coexposure of the high surface energy and more reactive {001} facets along with the low energy and thermodynamically stable {101} facets.

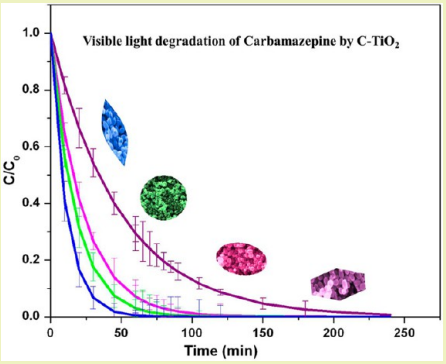

KEYWORDS: *Carbon loaded TiO_2, Microwave synthesis, Morphology control, Photocatalysis, Water pollution, Carbamazepine*

INTRODUCTION

Diverse morphological changes in semiconductor nanomaterials can be used for tuning their shape-dependent physical properties, which are consequently useful in applications, for instance, in photocatalysis. Titanium dioxide (TiO_2) is a popular photocatalytic material that has been utilized for a variety of applications.[1,2] Both theoretical and experimental studies have proven that the anatase phase of TiO_2 is better for photocatalysis than its rutile phase, due to the fast electron−hole recombination and lower surface activity in the latter. But, the large band gap (E_{gap} = 3.2 eV) of antase TiO_2 makes it active only in the UV region. Thus, several attempts have been made to shift the E_{gap} to the visible region.[3,4]

Doping is a strategy that is often employed for band gap engineering. It is well accepted that doped titania materials with their long-term stabilities and reduced E_{gap} values will find applications in solar light technologies.[5,6] In this regard, research is primarily focused on employing nonmetals as dopants.[7,8] Doping with carbon (C) and nitrogen (N) has attracted significant attention due to a reduction in potential traps for electron/hole recombination, in comparison with the metal dopants.[9−11] However, the photocatalytic efficiency of C-doped TiO_2 (C-TiO_2) under visible light is still low.[12] Doping of the TiO_2 lattice by C can take place either by substitution of Ti (C@Ti) or by substitution of oxygen (C@O). The corresponding lattice environments can be represented as C−O−Ti−O and Ti−C−Ti−O, respectively. Carbon incorporation on TiO_2 can happen either at anionic (oxygen) or cationic (Ti) sites, according to a theoretical study.[13] Experimental evidence are inadequate to precisely describe the type of incorporation.[14] One can achieve such understanding by making precise carbon environments including doping in the lattice, inclusion in the interstitial positions or deposition on the surface.[14,15] Through a density functional theory-based study, it was shown that C@O reduced E_{gap} of anatase TiO_2 by a small magnitude (0.08 eV) and also generated gap states that were C 2p in character.[13] In the band structure, these dopant states were found to be positioned between the valence and conduction bands of undoped TiO_2, based on which the shifts in optical absorption edge in C@O doped bulk TiO_2 and TiO_2 nanotubes could be understood. In comparison, C@Ti caused C 2s states to arise just below the original conduction band, so that the calculated E_{gap} was decreased to a value of 2.85 eV (compared to 3.2 eV of undoped anatase TiO_2) corresponding to the visible region.

Complete removal of pharmaceutically active compounds (PhACs) from an aquatic environment and drinking water is a major challenge today.[16] PhACs are found at an alarming rate in drinking water supplies around the world.[17] Although many advanced oxidation processes have been tested for the removal of PhACs,[18] semiconductor photocatalysis using TiO_2 is particularly attractive due to its higher pollutant removal

Received: January 20, 2015
Revised: May 15, 2015
Published: May 20, 2015

DOI: 10.1021/acssuschemeng.5b00044
ACS Sustainable Chem. Eng. 2015, 3, 1321−1329

efficiency, low cost, easy availability, nontoxicity, and easily modifiable properties.[19] Carbamazepine (CBZ), a common antiepileptic drug, is a persistent pollutant in wastewater. In a recent work, a sol−gel N-doped TiO_2 catalyst surface was reported to have shown enhancement in the photocatalytic removal efficiency of CBZ in visible light with increasing pH between 5 and 9.[20] For water spiked with 1 mg/L CBZ, a 45−70% CBZ removal was achieved within this pH range. Increasing alkalinity and natural organic matter was found to cause a significant reduction in CBZ removal capacity of the catalyst. The photocatalytic degradation efficiency also strongly decreased when using surface water and wastewater effluents as water sources.

Generally, efficiency of photocatalysis depends mainly on the surface area and the exposed planes, i.e., surface morphology of the catalyst. Average surface energies of the different facets of anatase TiO_2 predicted from theoretical calculations are as follows: {110} (1.09 J/m^2) > {001} (0.90 J/m^2) > {100} (0.53 J/m^2) > {101} (0.44 J/m^2).[21] Thus, extensive research is currently focused on the exposure of high surface energy facets of TiO_2, as these will have much higher chemical reactivity.[22−24] This lead to implications in photocatalysis-based environmental cleanup, water splitting hydrogen generation and solar energy as well as Li-ion batteries.[25]

In this work, C-TiO_2 was synthesized by a rapid technique for visible light photocatalytic applications. By changing the concentrations, in dilute conditions of the reactants, various morphologies, namely, spherical, distorted spherical, rice grain, and hexagonal shapes, were obtained. The photocatalytic activities of these morphologies of C-TiO_2 nanocrystals (NCs) toward CBZ were tested in the visible region, employing certain key parameters derived from the response surface methodology[26] for optimal removal efficiency.

EXPERIMENTAL SECTION

Sample Preparation. In a typical synthesis, a solution of 10 mM titaniumoxyacetylacetonate (TOAA) and 10 mM NH_4F was prepared in 50 mL of water. To the above solution was added 20 mg of glucose and then 10 mL of H_2O_2. The resultant mixture was stirred for 10 min and then subjected to microwave digestion. The as-synthesized materials were centrifuged, washed with water and methanol, and dried in an oven at 80 °C for 3 h. To remove the excess glucose, the as-synthesized samples were annealed at 350 °C for 2 h in a nitrogen atmosphere.

A number of solutions were prepared using different combinations of temperature, precursor concentration, reaction time, and volume of the microwave vessel. To understand the effect of these parameters individually, each was varied while keeping the other conditions constant. Table 1 lists the samples synthesized by using different concentrations of TOAA, NH_4F, and H_2O_2 under the same conditions of 80% volume of the Teflon vessel, 150 °C reaction temperature for 30 min and 400 W power. TiO_2 systems produced from variation of other parameters are listed in the Supporting Information, Tables S1−S3 along with the reaction conditions for each set.

Characterization. Powder X-ray diffraction (XRD) measurements were carried out using Bruker Discover D8 diffractometer with default background correction. Raman measurements were recorded using a WiTec GmbH, CRM αS300 instrument with 532 nm Nd:YAG laser line as an excitation source. High-resolution scanning electron microscopy (HRSEM) images were taken using a FEI Quanta FEG 200 with an EDS detector. High-resolution transmission electron microscopy (HRTEM) images were taken using a JEOL 3010 HRTEM instrument. Solid-state UV−vis measurements were performed by a Cary 5E UV−vis-NIR spectrophotometer. X-ray photoelectron spectroscopy (XPS) was carried out with an Omicron ESCA probe spectrometer with polychromatic Mg Kα X-rays ($h\nu$ = 1253.6 eV). The microwave digestion was done using the CEM Mars 5 microwave digester. The photocatalytic sample was analyzed by high performance liquid chromatography (HPLC) (Dionex, Ultimate 3000). The total organic carbon (TOC) content was measured utilizing the TOC analyzer, Shimadzu, Japan.

Table 1. Effect of Variation of Concentrations of TOAA, NH_4F, and H_2O_2, Keeping All Other Conditions[a] Fixed, on TiO_2 Morphology and Phase

sample code	TOAA (mM)	NH_4F (mM)	H_2O_2 (mM)	morphology	crystalline phase
CT-1	10	10	10	spherical	anatase
CT-2	10	20	10	distorted spherical	anatase
CT-3	10	10	0	no specific morphology	anatase
CT-4	10	60	10	spherical	anatase
CT-5	10	100	10	no specific morphology	anatase
CT-6	10	10	5	hexagonal	anatase
CT-7	10	10	15	elongated oval	anatase
CT-8	10	10	2.5	spherical	anatase
CT-9	5	10	10	rice grain	anatase
CT-10	5	10	5	spherical	anatase
CT-11	5	10	2.5	no specific morphology	anatase
CT-12	5	10	15	spherical	anatase
CT-21	30	10	10	spherical	anatase
CT-22	30	15	10	spherical	anatase

[a]Conditions: volume, 80%; temperature, 150 °C; time, 30 min; power, 400 W.

Photocatalytic Reaction. In a preceding study,[27] we have optimized the following parameters: catalyst concentration, pollutant concentration, light intensity, and time of reaction, for the degradation of CBZ by spherical C-TiO_2, utilizing visible light. To this end, 29 experiments were conducted and the system parameters were determined for optimal CBZ removal efficiency for all the C-TiO_2 morphologies presented herein.

For examining the photocatalytic removal of CBZ, each C-TiO_2 catalyst was suspended in CBZ solution of a desired concentration. Prior to irradiation, the solution was kept in the dark for 45 min to attain adsorption equilibrium (see the Supporting Information, Figure S1). Photocatalytic batch experiments were conducted in a cylindrical photochemical reactor of 400 mL volume, with a water circulation arrangement for maintaining the temperature between 25 and 30 °C. A 150 W high-pressure tungsten visible lamp (λ > 400 nm) was used for irradiation. Constant stirring with an oxygen flow rate of 300 mL/min was maintained throughout the experiment. Stock solution of the pollutant was prepared using ultrapure Millipore water. All intermediate samples were collected at regular intervals of time and analyzed using HPLC.

RESULTS AND DISCUSSION

Tuning Morphology by Different Parameters. More than 20 samples (listed in Table 1 and the Supporting Information, Tables S1−S3) were synthesized by varying the following parameters: temperature, reaction time, precursor concentration, and volume of the microwave vessel. The as-synthesized C-TiO_2 samples were subjected to SEM analysis. Figure 1 shows SEM images of samples CT-1, CT-2, CT-6, and CT-9. The CT-1 sample that was formed at a 1:1 ratio of TOAA:NH_4F exhibits a spherical morphology with a particle size of ∼50 nm. However, when the ratio was changed to 1:2 by reducing the TOAA concentration by half (keeping H_2O_2 volume fixed as for CT-1), the morphology changed from a spherical to rice grain shape (CT-9). At the same time, the

DOI: 10.1021/acssuschemeng.5b00044
ACS Sustainable Chem. Eng. 2015, 3, 1321−1329

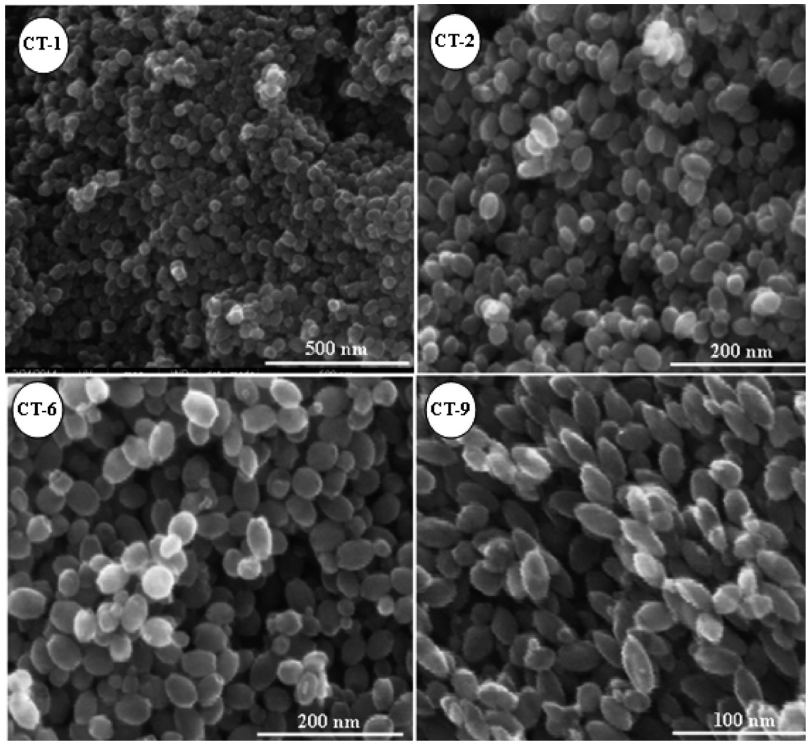

Figure 1. HRSEM images of (CT-1) spherical, (CT-2) distorted spherical, (CT-6) hexagonal, and (CT-9) rice grain shaped C-TiO_2 NCs.

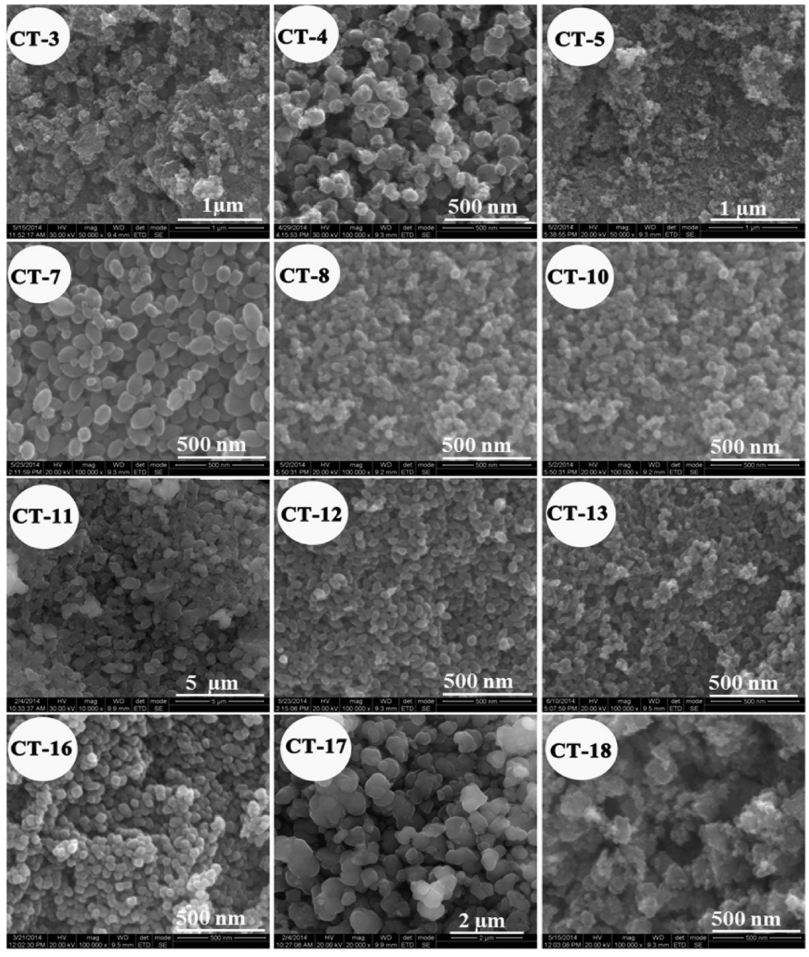

Figure 2. HRSEM images of C-TiO_2 samples prepared using different reaction conditions by microwave digestion technique.

DOI: 10.1021/acssuschemeng.5b00044
ACS Sustainable Chem. Eng. 2015, 3, 1321−1329

particle size further decreased to less than 50 nm. TOAA:NH_4F = 1:2 was also achieved by doubling the concentration of the NH_4F compared to that used for CT-1. This caused the morphology to change to a distorted spherical (CT-2) shape, along with an increase in particle size. On the other hand if a 1:1 ratio of TOAA:NH_4F was maintained, but the H_2O_2 concentration was decreased by 2-fold to 48.95 mM, an interesting hexagonal morphology was formed (CT-6). Elemental compositions of these four morphologies of C-TiO_2 are presented in the Supporting Information, Figure S2. The morphologies of the remaining C-TiO_2 samples that are listed in Table 1 are shown in Figure 2. However, use of high concentrations of the sources led to no specific morphology of C-TiO_2 with large particle sizes and poor shape control (see the Supporting Information, Figure S3).

The role of H_2O_2 has been found to be that of a structure directing or determining agent. No specific morphology was observed in the absence of H_2O_2 and varying its concentration greatly affected the particle size. Varying the reaction time but keeping the concentration of the precursors unchanged also affected the particle size. Microwave digestion for 18 min resulted in a distorted oval shape for C-TiO_2, which agglomerated with an increased particle size on extending the digestion time to 40 min. Varying the temperature, keeping other parameters constant, affected the morphology too. HRSEM images of C-TiO_2 illustrating the time and temperature dependence of synthesis are shown in the Supporting Information, Figure S4. It is noteworthy that irrespective of the reaction conditions, as given in Table 1 and the Supporting Information, Tables S1−S3, C-TiO_2 was always found in the anatase phase. This is confirmed by powder XRD, as displayed in the Supporting Information, Figure S5.

In the proceeding discussion, we will focus only on the results from the samples synthesized with low concentrations of TOAA and NH_4F, namely, the spherical (CT-1), distorted spherical (CT-2), hexagonal (CT-6), and rice grain (CT-9) shaped NC C-TiO_2 (refer to Table 1). HRTEM images (see Figure 3) confirmed the spherical shape of the CT-1 sample and yielded a particle size of ∼50 nm. The measured d value of 3.50 Å suggests the existence of a (101) plane in spherical C-TiO_2. In addition, the outer boundary (seen in Figure 3B, corresponding to CT-2) shows layers of carbon accumulated on the periphery. This can be confirmed by measuring EDS line scan of a single spherical shaped C-TiO_2, as given in the Supporting Information, Figure 6. This confirms that carbon is accumulated on the surface. However, there is significant C content in the particle, which is uniform. This carbon is likely to be due to doping. The distorted spherical morphology of CT-2 is easily visible from the figure, with clear lattice fringes at an interplanar distance of 3.51 Å, due to the (101) plane as in CT-1.[28] The corresponding particle size was calculated to be ∼40−50 nm. The HRTEM image of CT-6 sample clearly exhibits six vertices and a hexagonal morphology in which four sides are long and two are short. Each short side was found to be 10 nm in length, while the remaining sides were measured to be 20 nm in length. The average particle size was found to be 40 nm and was further confirmed by the Scherer formula from XRD. As in the previous two samples, for CT-6 also the measured *d* spacing was found to be 3.51 Å corresponding to a (101) plane. The electron microscopy images of CT-9 showcase the presence of two vertices in each particle with a rice grain shape. From the SEM measurements, a particle size of ∼40−50 nm was derived for CT-9. The lattice fringes reveal

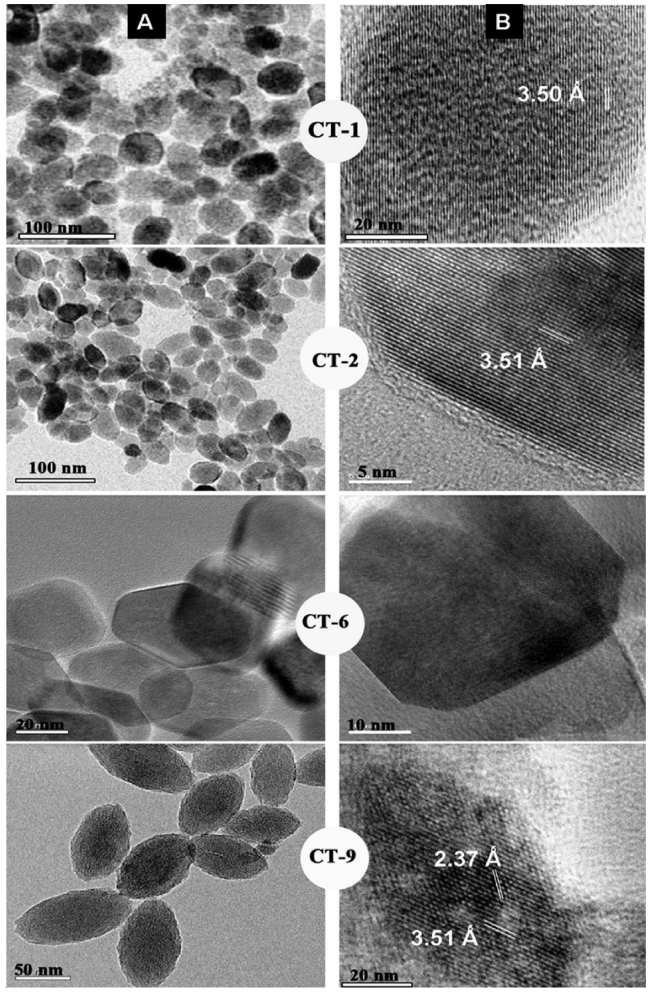

Figure 3. TEM images at (A) low and (B) high magnification of spherical (CT-1), distorted spherical (CT-2), hexagonal (CT-6), and rice grain (CT-9) shaped of C-TiO_2 NCs.

a clear crystallinity and an arrangement of atoms with interplanar distances of 2.37 Å and 3.50 Å corresponding to (004) and (101) planes, respectively of anatase TiO_2. Interestingly, only very few boundary layers (thin layers) of carbon were present in CT-6 and CT-9 samples when compared with CT-1 and CT-2 samples, showcasing that the carbon thickness changes with the sample. More HRTEM images of these four morphologies of C-TiO_2 can be found in the Supporting Information, Figure S7.

Structural Elucidation of C-TiO_2 with Different Morphologies. The powder XRD profiles of the four morphologies of C-TiO_2 are depicted in Figure 4. It is deduced that all the materials index exactly to the anatase phase of bulk TiO_2. The peak at 2θ = 25.1° is due to the (101) plane of anatase TiO_2, while other peaks correspond to the (103), (004), (112), (200), (105), (211), and (204) planes of bulk TiO_2 (JCPDS 89-4921). Though there is a small deviation in the peak positions of the four samples with respect to the bulk form due to carbon accumulation, there are no significant changes in these within the different morphologies of C-TiO_2. However, the full width at half-maxima (fwhm) of any peak (plane) is not the same due to the difference in particles sizes of the four shapes.

Bulk anatase TiO_2 is known to exhibit six Raman active modes (three E_g, two B_{1g} and one A_{1g}).[29] These spectral

DOI: 10.1021/acssuschemeng.5b00044
ACS Sustainable Chem. Eng. 2015, 3, 1321−1329

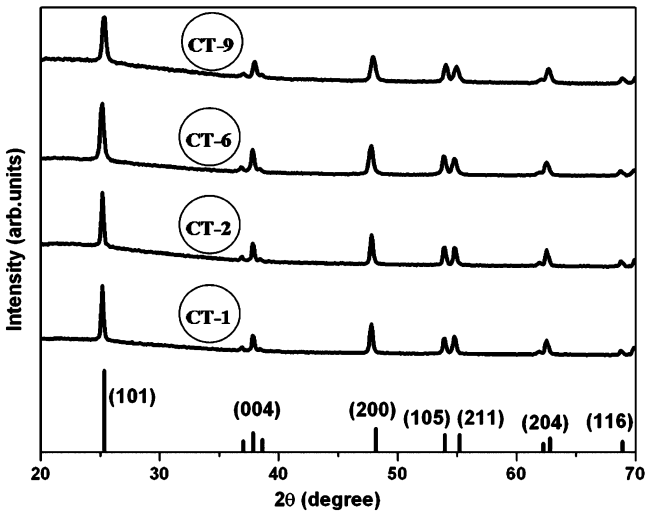

Figure 4. XRD profiles of the four different morphologies of C-TiO_2. For comparison, XRD of bulk anatase TiO_2 is plotted in the bottom (JCPDS 89-4921).

features can also be seen in the low frequency region of the Raman spectra of the four C-TiO_2 NCs displayed in Figure 5A. Thus, in agreement with the XRD analysis, Raman spectroscopy also confirms that these systems were in the anatase phase. The strong phonon peak at 150 cm^{-1} corresponds to an E_g mode, but its position is shifted by ~6−8 cm^{-1} relative to bulk TiO_2, possibly due to C content. The peaks at ~400, 510, and 620 cm^{-1} index well to the B_{1g}, A_{1g}, and E_g modes, respectively. The spectral feature in the high frequency region (see Figure 5B) consists of D and G bands which are normally observed at ~1350 and 1585 cm^{-1}, respectively. These bands correspond to sp^2 carbon atoms in a disordered (D) environment and to carbons in extended p conjugated graphite-like (G) arrangements. This carbonaceous region upon deconvolution reveals that the disordered character of the D band at 1357 cm^{-1} is higher in intensity than the graphitic character of the G band at 1585 cm^{-1}.

The ratio of the intensities of the D and G bands (I_D/I_G) or the degree of graphitization is an indication of the amount of graphitic carbon formed at the surface of the nanoparticle; lower the I_D/I_G ratio, higher the degree of graphitization.[30,31] I_D/I_G was found to be 2.15, 2.06, 1.98, and 1.97, respectively for the distorted spherical, spherical, rice grain, and hexagonal shaped C-TiO_2. These values are greater than the I_D/I_G ratios (1.06−1.66) of previously reported[32] C-TiO_2 and are therefore indicative of the presence of lesser graphitic carbon in our samples. It can be further noticed that the I_D/I_G ratio of the rice grain and hexagonal shaped C-TiO_2 is lower than that of the spherical and distorted spherical shaped C-TiO_2. As the D band is reflective of disorder/structural defects, based on I_D, the disorder is likely to be less in the first pair of samples and high in the second pair of C-TiO_2 NCs.

The UV−vis diffuse reflectance spectra of CT-1, CT-2, CT-6, and CT-9 are presented in the Supporting Information, Figure S8. Although P25 Degussa (bulk TiO_2) showed an absorption onset in the UV region, the absorption of all morphologies of C-TiO_2 exhibited a shoulder in the visible region. Absorbance is enhanced with increasing carbon content as follows: distorted spherical > spherical > hexagonal > rice grain shaped C-TiO_2. This trend is in agreement with the TOC results, according to which the percentages of carbon in the distorted spherical (CT-2), spherical (CT-1), hexagonal (CT-6), and rice grain (CT-9) shaped C-TiO_2 samples were 3.35, 2.95, 2.68, and 2.55%, respectively.

Carbon in TiO_2 Network. The carbon environment in the four different morphologies of C-TiO_2 was monitored by XPS, and the results are shown in Figure 6. For comparison, XPS of bulk TiO_2 (P25 Degussa) is also plotted. It can be seen from the figure that after deconvolution, C 1s appears as three distinct peaks at 284.6, 286.3, and 288.5 eV, which are due to adventitious carbon species. The first peak at 284.6 eV is due to graphitic carbon formed at the surface of the nanoparticle, whereas the latter two arise from the C—OH (and C—O—C) and C═O (and COO) bonds of the carbonate-like species due to oxidized carbon species. This carbon species (carbonate-like) are likely to be substituting the Ti site or sitting in interstitial positions.[33−36,14] The presence of C—O in the TiO_2 was

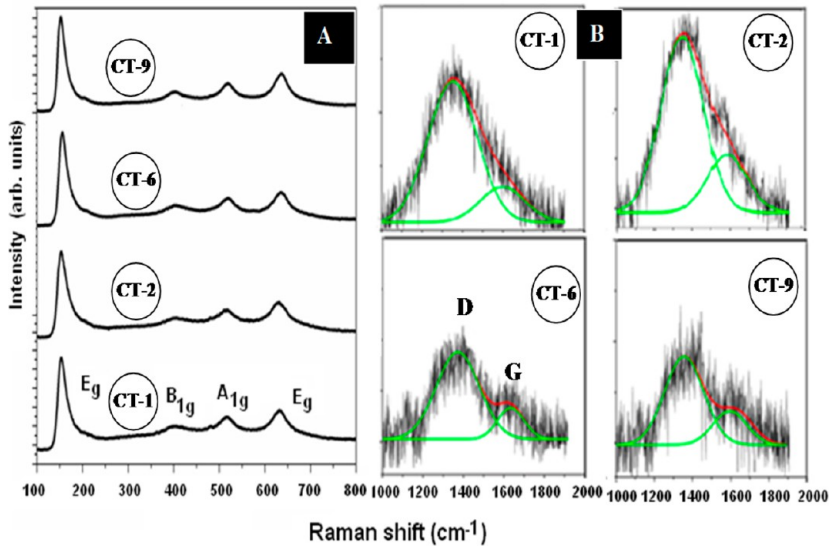

Figure 5. Raman profiles of the spherical (CT-1), distorted spherical (CT-2), hexagonal (CT-6), and rice grain (CT-9) shaped C-TiO_2. (A) TiO_2 bands in the low frequency region; (B) D and G bands in the higher frequency region.

DOI: 10.1021/acssuschemeng.5b00044
ACS Sustainable Chem. Eng. 2015, 3, 1321−1329

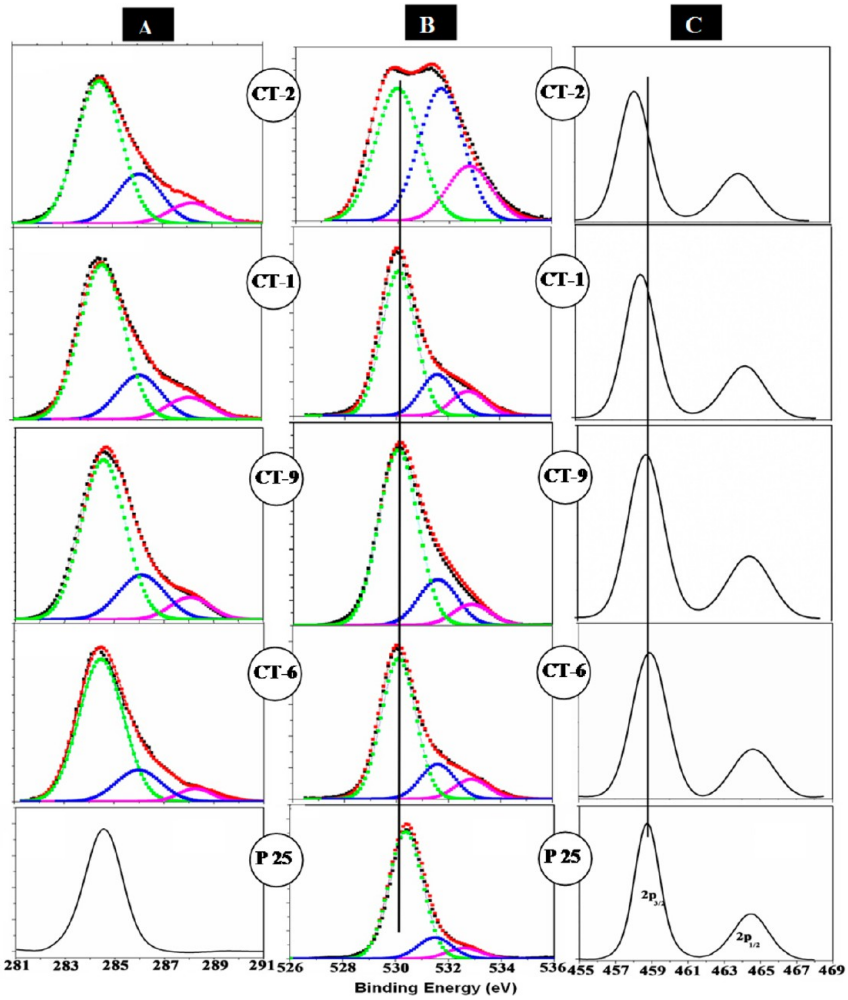

Figure 6. XPS of CT-1, CT-2, CT-6, and CT-9 C-TiO_2 samples. For comparison, XPS of bulk TiO_2 (P25 Degussa) is plotted in the bottom. (A) C 1s, (B) O 1s, and (C) Ti 2p. Color scheme: black-experimental curve; red-fitted; green, blue, and pink-deconvoluted species.

further confirmed by infrared spectra (see the Supporting Information, Figure S9), which exhibit a peak at 1059 cm^{-1} due to C—O stretching.

Of the three peaks in Figure 6A, intensity of the one due to carbonate-like feature changed with the morphology of C-TiO_2. The measured intensity of this peak at 286.3 eV follows the order: distorted spherical > spherical > hexagonal > rice grain C-TiO_2. This trend is in agreement with the calculated total percentage of carbon from the TOC measurement, mentioned in the previous section. In addition, the absence of a peak around 282.0 eV confirms that the carbon did not substitute oxygen in the lattice.[37] The intensity of the 284.6 eV peak implies that the percentage of graphitic carbon is high in the distorted spherical C-TiO_2 and low in the hexagonal C-TiO_2. The uniform C content due to doping within the TiO_2 particle, as proposed from the SEM-EDS line scan, could not be seen distinctly in XPS.

The Ti 2p XPS peak of P25 Degussa in Figure 6C consists of two energy levels of Ti $2p_{1/2}$ and $2p_{3/2}$ at 464 and 458 eV, respectively with a separation of ~5.8 eV.[38] Two observations are easily noticeable from panel C: (i) the peak shift (with respect to P25 Degussa) toward lower energy is maximum for the distorted spherical C-TiO_2 and is relatively much greater than for other systems and (ii) the distorted spherical morphology exhibits lower line-width than the others. The fact that the Ti 2p peak position differs for four different morphologies along with the nature of C accumulation on the TiO_2 surface. Thus, the hexagonal and rice grain shaped C-TiO_2 show only a subtle change from the standard TiO_2, whereas the distorted spherical and spherical shapes show greater differences in energy positions. Overall, the distorted spherical C-TiO_2 shows a deviation of nearly 0.45 eV from P25 Degussa, indicative of a partial charge transfer from the surface carbon moiety to the Ti^{4+} centers in the TiO_2 network.[39]

The XPS for O 1s (Figure 6B) shows three different environments in C-TiO_2 for all the four morphologies. The peak positions at 530.3, 531.5, and 532.8 eV in P25 Degussa can be ascribed to Ti—O (O^{2-} lattice oxygen), surface −OH, and adsorbed H_2O, respectively, whereas the peak positions at 530.1, 531.5, and 532.9 eV in all the C-TiO_2 NCs are indexed to Ti—O (O^{2-} lattice oxygen), C═O (and COO), and C—OH (and C—O—C) species, respectively.[39,40] The enhancement of C═O and C—OH signals in the distorted spherical morphology suggested increased hydration (OH and/or H_2O) with an increase of deposited carbon content (i.e., increased line-width) revealed by the C 1s spectra. The shifting (by 0.2 eV) of the lattice oxygen peak at 530.1 eV in all the C-TiO_2 toward lower energy, relative to the P25 Degussa standard, is indicative of C accumulation.

DOI: 10.1021/acssuschemeng.5b00044
ACS Sustainable Chem. Eng. 2015, 3, 1321−1329

The Brunauer–Emmett–Teller (BET) surface area data for the four morphological samples are presented in the Supporting Information, Table S4. The BET results show that the C-TiO_2 systems have different surface areas, pore volumes, and pore diameters. Their N_2 adsorption–desorption isotherms are displayed in the Supporting Information, Figure S10. The spherical morphology (CT-1) of C-TiO_2 shows a sharp decline in the desorption branch indicating its mesoporosity, whereas the hysteresis (Type-IV, H1) between the two curves suggests the pores to have a diffusion bottleneck structure.[41] The following parameters were estimated for CT-1: surface area 62 m^2/g, pore volume 0.24 cc/g, and BJH pore diameter 18.0 nm. In addition, it showed a unimodal pore size distribution that was a little broad in the range due to its spherical morphology. The reason for the high pore volume may be the fusion of microvoids into macro voids during crystallization. The distorted spherical sample (CT-2) is predicted to have a surface area (61 m^2/g) similar to that of the CT-1 sample, but with a smaller pore volume and larger average pore diameter of 0.19 cc/g and 22.4 nm, respectively. CT-2 was found to have two additional pores of sizes 3.6 and 58.6 nm, implying that distorted spherical condensation led to the formation of lower range of mesopores and also macropores due to surface aggregation of these particles. Furthermore, the presence of H3 hysteresis implies nonrigid aggregation of plate-like particles that expose slit-shaped pores.

For the hexagonal shaped C-TiO_2 (CT-6), a type-II isotherm with a still lower surface area of 33 m^2/g was observed, with a pore volume and pore diameter of 0.18 cc/g and 19.0 nm, respectively. The BJH pore size distribution exhibits sharp unimodal pores, which are the probable reason for the heterogeneous uptake of carbon and increased pore shrinkage in the region of particle aggregation. Interestingly, the rice grain morphology (CT-9) shows a type-IV isotherm with H4 hysteresis loop and a relatively higher surface area of 229 m^2/g with a pore volume of 0.17 cc/g and BJH pore diameter of 3.6 nm. On the basis of the smooth rise in the pore condensation for CT-9, it can be inferred that uniform pores are present, whereas overall results suggest the existence of ordered narrow slit-like mesoporous pores in the micropore region due to the gradual decomposition of carbon.

Photocatalytic Degradation of CBZ. We have previously examined the spherical shaped C-TiO_2 for the photocatalytic degradation of carbamazepine, an emerging contaminant in water. Details of the study and the conditions derived for optimal removal of CBZ are discussed elsewhere.[27] Using these optimized parameters (catalyst concentration of 230 mg/L, light intensity of 7700 lux and pollutant concentration of 50 μg/L), the visible light photocatalytic degradation of CBZ was carried out by all four morphologies of C-TiO_2. Additional control experiments were done on undoped TiO_2 and carbon prepared by the same method (CT-1 method). It was found that degradation occurred slowly for both carbon and TiO_2, as shown in the Supporting Information, Figure S11.

As can be seen from Figure 7, the time taken to degrade CBZ using the rice grain, spherical, distorted spherical, and hexagonal shaped C-TiO_2 was 85, 120, 210, and 240 min, respectively. The reaction rates, k (min^{-1}), were determined by plotting $\ln(C/C_0)$ versus time, where C = concentration after time t has elapsed and C_0 = original concentration at t = 0. All these trials were found to follow first-order kinetics with a R^2 value of more than 0.90 (see the Supporting Information, Table S5). The rate of CBZ degradation was much faster with the rice

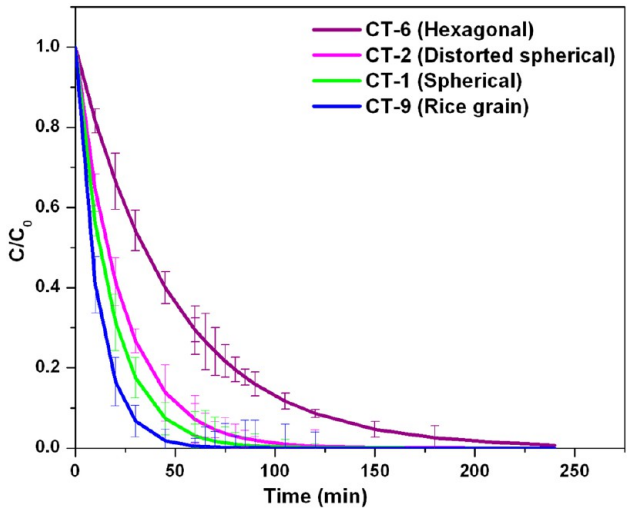

Figure 7. Degradation of carbamazepine by different morphologies of C-TiO_2NCs.

grain shaped C-TiO_2 catalyst than with the other three catalysts. This photocatalytic behavior corroborates well with surface area measurements. The measured surface area (see the Supporting Information, Table S4) is found to be rather large in the rice grain C-TiO_2 (229 m^2/g) compared to in the spherical (62 m^2/g), distorted spherical (61 m^2/g), and hexagonal (33 m^2/g) C-TiO_2. Thus, it can be inferred that the high surface area of the rice grain C-TiO_2 is responsible for its high photocatalytic activity.

Chemical Control of Morphology. Our study (tuning morphology by different parameters, vide supra) revealed that low concentrations of H_2O_2 and NH_4F played major roles in controlling morphology and determining the size of C-TiO_2, and it is expected that there may be a competition between them.[42] F^- ions are well-known for their role as etching agents and F^- ions from NH_4F can influence the crystallization and growth of TiO_2 due to rapid in situ dissolution and recrystallization.[43,44] Thus, when H_2O_2 concentration is reduced by 2-fold (to 5 mL) compared to that in the spherical CT-1, the F^- ions etch anisotropically leading to the hexagonal shaped C-TiO_2 (CT-6) with clear vertices. We postulate that in all the C-TiO_2 morphologies, this anisotropic etching probably causes the exposure of the (101) plane that has the lowest surface energy. At the same time, the role of H_2O_2[45] is also crucial, as it was impossible to get the distinct morphologies in its absence. The adsorption of peroxide ions form various intermediate complexes viz., $[Ti(O_2)_2(OH_2)OOH]^-$, and/or $[Ti(O_2)_2(OH_2)OOH_2]$, etc., and can lower the surface energy of {001} facets, but these get exposed only in the rice grain shaped C-TiO_2 due to the lower concentration of TOAA.

An interesting observation was noted in the surface morphology of four differently shaped C-TiO_2. In principle, the lower surface energy planes (101), (004), and (200) correspond to the most displayed facets of {101}, {001}, and {100}, respectively in natural anatase crystals.[46,47] All the four morphologies of C-TiO_2 show the (101) plane of the {101} facet in electron microscopy images. Interestingly, the rice grain shaped C-TiO_2 has coexposed {001} and {101} facets for (004) and (101) planes, respectively as understood from electron microscopy images. Roy et al.[48] confirmed the presence of high energy {001} reductive facets with low energy {101} oxidative facets of TiO_2 as being responsible for efficient

DOI: 10.1021/acssuschemeng.5b00044
ACS Sustainable Chem. Eng. 2015, 3, 1321–1329

photocatalytic degradation of a dye. Thus, in our work, the enhanced photocatalytic activity of the rice grain shaped C-TiO_2 could be due to the coexposure of the {001} and {101} facets, as deduced from its TEM images in Figure 3. Different morphologies of TiO_2 have been reported to show mostly {001} facets with enhanced photocatalytic applications even when synthesized using F^- ions.[49,50] Though F^- ions have been used for preparing C-TiO_2 in this work, in a given diluted condition ([TOAA/2]), the rice grain C-TiO_2 alone had coexposed {001} and {101} facets due to an competition between F^- and H_2O_2. However, a detailed mechanistic study is needed to understand the real factors responsible.

CONCLUSIONS

Various C-TiO_2 morphologies were synthesized by a rapid microwave digestion method. The morphologies were significantly tuned at low concentrations of the precursors for synthesizing anatase C-TiO_2. Among the four different morphologies, the rice grain shaped C-TiO_2 showed enhanced visible light degradation of carbamazepine, a pharmaceutical pollutant in wastewater, due to the presence of coexposed low energy/high energy {101}/{001} facets and its high surface area. These newly synthesized carbon enriched TiO_2 NCs may find useful in applications such as water splitting. Precise understanding of the nature of carbon in these materials needs additional studies.

ASSOCIATED CONTENT

Supporting Information

List of reaction parameters in Tables S1−S4, EDS profile in Figure S2, SEM images at different synthetic parameters (Figures S3 and S4), XRD profiles at various experimental parameters (Figure S5), EDS line scan mapping for CT-1 in Figure S6, HRTEM, UV−vis and FT-IR for samples CT-1 to CT-4 in Figures S7, S8, and S9 respectively, BET surface area results in Figure S10 and Table S4, and rates for photocatalytic CBZ degradation for CT-1 to CT-4 in Table S5 and controlled experiments result found in Figures S1 and S11. This material is available free of charge via the Internet at http://pubs.acs.org/ .The Supporting Information is available free of charge on the ACS Publications website at DOI: 10.1021/acssuschemeng.5b00044.

AUTHOR INFORMATION

Corresponding Author

*T. Pradeep. E-mail: pradeep@iitm.ac.in.

Notes

The authors declare no competing financial interest.

ACKNOWLEDGMENTS

We thank the Department of Science and Technology, Government of India for financial support. B.S. acknowledges the Indian Institute of Technology Madras for an Institute Postdoctoral Fellowship.

REFERENCES

(1) Daghrir, R.; Drogui, P.; Robert, D. Modified TiO_2 for environmental photocatalytic applications: A review. *Ind. Eng. Chem. Res.* **2013**, *52*, 3581−3599.
(2) Carp, O.; Huisman, C. L.; Reller, A. Photoinduced reactivity of titanium dioxide. *Prog. Solid State Chem.* **2004**, *32*, 33−177.
(3) Dette, C.; Pérez-Osorio, M. A.; Kley, C. S.; Punke, P.; Patrick, C. E.; Jacobson, P.; Giustino, F.; Jung, S. J.; Kern, K. TiO_2 anatase with a bandgap in the visible region. *Nano Lett.* **2014**, *14*, 6533−6538.
(4) Dong, J.; Han, J.; Liu, Y.; Nakajima, A.; Matsushita, S.; Wei, S.; Gao, W. Defective black TiO_2 synthesized via anodization for visible-light photocatalysis. *ACS Appl. Mater. Interfaces* **2014**, *6*, 1385−1388.
(5) Zha, C.; Shen, L.; Zhang, X.; Wang, Y.; Korgel, B. A.; Gupta, A.; Bao, N. Double-sided brush-shaped TiO_2 nanostructure assemblies with highly ordered nanowires for dye-sensitized solar cells. *ACS Appl. Mater. Interfaces* **2014**, *6*, 122−129.
(6) Braham, R. J.; Harris, A. T. Review of major design and scale-up considerations for solar photocatalytic reactors. *Ind. Eng. Chem. Res.* **2009**, *48*, 8890−8905.
(7) Zhang, J.; Wu, Y.; Xing, M.; Leghari, S. A. K.; Sajjad, S. Development of modified N-doped TiO_2 photocatalyst with metals, nonmetals and metal oxides. *Energy Environ. Sci.* **2010**, *3*, 715−726.
(8) Chen, D.; Jiang, Z.; Geng, J.; Wang, Q.; Yang, D. Carbon and nitrogen co-doped TiO_2 with enhanced visible-light photocatalytic activity. *Ind. Eng. Chem. Res.* **2007**, *46*, 2741−2746.
(9) Qian, W.; Alex Greaney, P.; Fowler, S.; Chiu, S. K.; Goforth, A. M.; Jiao, J. Low-temperature nitrogen doping in ammonia solution for production of N-doped TiO_2-hybridized graphene as a highly efficient photocatalyst for water treatment. *ACS Sustainable Chem. Eng.* **2014**, *2*, 1802−1810.
(10) Irie, H.; Watanabe, Y.; Hashimoto, K. Carbon-doped anatase TiO_2 powders as a visible light sensitive photocatalyst. *Chem. Lett.* **2003**, *32*, 772−773.
(11) Khan, S. U. M.; Al-Shahry, M.; Ingler, W. B., Jr. Efficient photochemical water splitting by a chemically modified N-TiO_2. *Science* **2002**, *297*, 2243−2245.
(12) Ohno, T.; Miyamoto, Z.; Nishijima, K.; Kanemitsu, H.; Feng, X. Y. Sensitization of photocatalytic activity of S- or N-doped TiO_2 particles by adsorbing Fe^{3+} cations. *Appl. Catal., A* **2006**, *302*, 62−68.
(13) Yang, K.; Dai, Y.; Huang, B.; Whangbo, M.-H. Density functional characterization of the visible-light absorption in substitutional C-anion- and C-cation-doped TiO_2. *J. Phys. Chem. C* **2009**, *113*, 2624−2629.
(14) Zhang, L.; Tse, M. S.; Tan, O. K.; Wang, Y. X.; Han, M. Facile fabrication and characterization of multi-type carbon-doped TiO_2 for visible light-activated photocatalytic mineralization of gaseous toluene. *J. Mater. Chem. A* **2013**, *1*, 4497−4507.
(15) Wang, S.; Zhao, L.; Bai, L.; Yan, J.; Jiang, Q.; Lian, J. Enhancing photocatalytic activity of disorder engineered C/TiO_2 and TiO_2 nanoparticles. *J. Mater. Chem. A* **2014**, *2*, 7439−7445.
(16) Kaplan, R. Review: Pharmacological pollution in water. *Crit. Rev. Environ. Sci. Technol.* **2013**, *43*, 1074−1116.
(17) Benner, J.; Helbling, D. E.; Kohler, H. -P. E.; Wittebol, J.; Kaiser, E.; Prasse, C. Is biological treatment a viable alternative for micropollutant removal in drinking water treatment processes? *Water Res.* **2013**, *47*, 5955−5976.
(18) Brillas, E.; Sirés, I.; Oturan, M. Electro-Fenton process and related electrochemical technologies based on Fenton's reaction chemistry. *Chem. Rev.* **2009**, *109*, 6570−631.
(19) Fujishima, A.; Rao, T. N.; Tryk, D. A. Titanium dioxide photocatalysis. *J. Photochem. Photobiol., C* **2000**, *1*, 1−21.
(20) Avisar, D.; Horovitz, I.; Lozzi, L.; Ruggieri, F.; Baker, M.; Abel, M. L.; Mamane, H. Impact of water quality on removal of carbamazepine in natural waters by N-doped TiO_2 photocatalytic thin film surfaces. *J. Hazard Mater.* **2012**, *244−245*, 463−471.
(21) Lazzeri, M.; Vittadini, A.; Selloni, A. Structure and energetics of stoichiometric TiO_2 anatase surfaces. *Phys. Rev. B* **2001**, *63*, 155409.
(22) Han, X.; Kuang, Q.; Jin, M.; Xie, Z.; Zheng, L. Synthesis of titania nanosheets with a high percentage of exposed (001) facets and related photocatalytic properties. *J. Am. Chem. Soc.* **2009**, *131*, 3152−3153.
(23) Liu, S.; Yu, J.; Jaroniec, M. Anatase TiO_2 with dominant high-energy {001} facets: Synthesis, properties, and applications. *Chem. Mater.* **2011**, *23*, 4085−4093.

DOI: 10.1021/acssuschemeng.5b00044
ACS Sustainable Chem. Eng. 2015, 3, 1321−1329

(24) Lee, W.-J.; Sung, Y.-M. Synthesis of anatase nanosheets with exposed (001) facets via chemical vapor deposition. *Cryst. Growth Des.* **2012**, *12*, 5792−5795.
(25) Liu, S.; Yu, J.; Jaroniec, M. Anatase TiO_2 with dominant high-energy {001} facets: Synthesis, properties, and applications. *Chem. Mater.* **2011**, *23*, 4085−4093.
(26) Vaez, M.; Moghaddam, A. Z.; Alijani, S. Optimization and modeling of photocatalytic degradation of azo dye using a response surface methodology (RSM) based on the central composite design with immobilized titania nanoparticles. *Ind. Eng. Chem. Res.* **2012**, *51*, 4199−4207.
(27) We have optimized CBZ removal efficiency using spherical shaped C-TiO_2. The result is unpublished.
(28) Neville, E. M.; Mattle, M. J.; Loughrey, D.; Rajesh, B.; Rahman, M.; Don MacElroy, J. M.; Sullivan, J. A.; Thampi, K. R. Carbon-doped TiO_2 and carbon, tungsten-codoped TiO_2 through sol−gel processes in the presence of melamine borate: Reflections through photocatalysis. *J. Phys. Chem. C* **2012**, *116*, 16511−16521.
(29) Shen, J.; Wang, H.; Zhou, Y.; Ye, N.; Li, G.; Wang, L. Anatase/rutile TiO_2 nanocomposite microspheres with hierarchically porous structures for high-performance lithium-ion batteries. *RSC Adv.* **2012**, *2*, 9173−9178.
(30) Foong, Y. M.; Koh, A. T. T.; Ng, H. Y.; Chua, D. H. C. Mechanism behind the surface evolution and microstructure changes of laser fabricated nanostructured carbon composite. *J. Appl. Phys.* **2011**, *110*, 054904.
(31) Hu, Z.; Yan, Z.; Shen, P. K.; Zhong, C.-J. Nano-architectures of ordered hollow carbon spheres filled with carbon webs by template-free controllable synthesis. *Nanotechnology* **2012**, *23*, 485404.
(32) Wang, Y.; Shi, R.; Lin, J.; Zhu, Y. Significant photocatalytic enhancement in methylene blue degradation of TiO_2 photocatalysts via graphene-like carbon in situ hybridization. *Appl. Catal., B* **2010**, *100*, 179−183.
(33) Kiran, V.; Sampath, S. Enhanced Raman spectroscopy of molecules adsorbed on carbon-doped TiO_2 obtained from titanium carbide: A visible-light-assisted renewable substrate. *ACS Appl. Mater. Interfaces* **2012**, *4*, 3818−3828.
(34) Liu, J.; Zhang, Q.; Yang, J.; Ma, H.; Tade, M. O.; Wang, S.; Liu, J. Facile synthesis of carbon-doped mesoporous anatase TiO_2 for the enhanced visible-light driven photocatalysis. *Chem. Commun.* **2014**, *50*, 13971−13974.
(35) Liu, B.; Liu, L.-M.; Lang, X.-F.; Wang, H.-Y.; Lou, X. W.; Aydil, E. S. Doping high-surface-area mesoporous TiO_2 microspheres with carbonate for visible light hydrogen production. *Energy Environ. Sci.* **2014**, *7*, 2592−2597.
(36) Cao, X. P.; Li, D.; Jing, W. H.; Xing, W. H.; Fan, Y. Q. Synthesis of visible-light responsive C, N and Ce co-doped TiO_2 mesoporous membranes via weak alkaline sol−gel process. *J. Mater. Chem.* **2012**, *22*, 15309−15315.
(37) Wang, H.; Wu, Z.; Liu, Y. A simple two-step template approach for preparing carbon-doped mesoporous TiO_2 hollow microspheres. *J. Phys. Chem. C* **2009**, *113*, 13317−13324.
(38) Zhou, W.; Liu, Y.; Zhang, Y.; Yang, G.; Deng, S.; Shen, F.; Peng, H.; Wang, L. Novel multi-layer cross-linked TiO_2/C nanosheets and their photocatalytic properties. *New J. Chem.* **2014**, *38*, 1647−1654.
(39) Lin, C.; Song, Y.; Cao, L.; Chen, S. Effective photocatalysis of functional nanocomposites based on carbon and TiO_2 nanoparticles. *Nanoscale* **2013**, *5*, 4986−4992.
(40) Zhong, J.; Chen, F.; Zhang, J. Carbon-deposited TiO_2: Synthesis, characterization, and visible photocatalytic performance. *J. Phys. Chem. C* **2010**, *114*, 933−939.
(41) Olsen, R. E.; Alam, T. M.; Bartholomew, C. H.; Enfield, D. B.; Woodfield, B. F. Structure analysis of Al-modified TiO_2 nanocatalyst supports. *J. Phys. Chem. C* **2014**, *118*, 9176−9186.
(42) Cai, J.; Wang, Z.; Lv, K.; Zheng, Y.; Yu, J.; Li, M. Rapid synthesis of a TiO_2 hollow microsphere assembly from hollow nanoparticles with enhanced photocatalytic activity. *RSC Adv.* **2013**, *3*, 15273−15281.
(43) Liu, N.; Mirabolghasemi, H.; Lee, K.; Albu, S. P.; Tighineanu, A.; Altomare, M.; Schmuk, P. Anodic TiO_2 nanotubes: Double walled vs. single walled. *Faraday Discuss.* **2013**, *164*, 107−116.
(44) Yu, J. G.; Yu, H.; Cheng, B.; Zhao, X.; Yu, J. C.; Ho, W. The effect of calcination temperature on the surface microstructure and photocatalytic activity of TiO_2 thin films prepared by liquid phase deposition. *J. Phys. Chem. B* **2003**, *107*, 13871−13879.
(45) Li, T.; Tian, B.; Zhang, J.; Dong, R.; Wang, T.; Yang, F. Facile tailoring of anatase TiO_2 morphology by use of H_2O_2: From microflowers with dominant {101} facets to microspheres with exposed {001} facets. *Ind. Eng. Chem. Res.* **2013**, *52*, 6704−6712.
(46) Ramamoorthy, M.; Vanderbit, D.; King-Smith, R. D. First-principle calculations of the energetics of stoichiometric TiO_2 surfaces. *Phys. Rev. B* **1994**, *49*, 16721−16727.
(47) Diebold, U. The surface science of titanium dioxide. *Surf. Sci. Rep.* **2003**, *48*, 53−229.
(48) Roy, R.; Sohn, Y.; Pradhan, D. Synergy of low-energy {101} and high-energy {001} TiO_2 crystal facets for enhanced photocatalysis. *ACS Nano* **2013**, *7*, 2532−2540.
(49) Dozzi, M. V.; Selli, E. Specific facets-dominated anatase TiO_2: Fluorine-mediated synthesis and photoactivity. *Catalysts* **2013**, *3*, 455−485.
(50) Gu, L.; Wang, J.; Cheng, H.; Zhao, Y.; Liu, L.; Han, X. One-step preparation of graphene-supported anatase TiO_2 with exposed {001} facets and mechanism of enhanced photocatalytic properties. *ACS Appl. Mater. Interfaces* **2013**, *5*, 3085−3093.

DOI: 10.1021/acssuschemeng.5b00044
ACS Sustainable Chem. Eng. 2015, 3, 1321−1329